Visualizing flux distribution of superconductors in external magnetic fields with magnetic force microscopy

U. H. Pi, A. Schwarz, M. Liebmann,* and R. Wiesendanger
Institute of Applied Physics and Microstructure Research Center, University of Hamburg, Jungiusstrasse 11, 20355 Hamburg, Germany

Z. G. Khim
School of Physics, Seoul National University, Seoul 151-742, South Korea

D. H. Kim
Department of Physics, Yeungnam University, Kyungsan, South Korea
(Received 2 December 2005; published 7 April 2006)

We visualized the flux distribution of a $Bi_2Sr_2CaCu_2O_{8+\delta}$ single crystal in transversal geometry by using low temperature magnetic force microscopy in the dynamic mode. With increasing external magnetic field, the magnetic flux density exhibited a distribution, which generally followed the Bean model. When the propagating flux front passed through the imaging area, we could observe a shift of the magnetic force microscopy signal toward an unexpected direction. The origin of this shift was studied by considering very long-range magnetic force due to the specific flux and current distribution near the propagating flux front.

DOI: 10.1103/PhysRevB.73.144505 PACS number(s): 74.25.Qt, 68.37.Rt

I. INTRODUCTION

The magnetic behavior in the mixed state of high temperature superconductors has been of considerable scientific and technological interest. For example, the dynamics of vortices affect the transport properties of superconductors. A direct observation of the magnetic flux distribution is expected to contribute to a better understanding of the properties of superconductors.

Magnetic force microscopy (MFM) has achieved single vortex resolution.[1–3] All these MFM investigations have been conducted in the low flux density regime, where individual vortices can be easily distinguished as objects with radii on the order of the London penetration depth λ. However, MFM can also be operated under high external fields and we have demonstrated that higher density flux distribution (intervortex distance $r<\lambda$) can be studied.[4]

In this paper, we report about our investigation on the MFM visualization of the flux distribution in transversal geometry of a $Bi_2Sr_2CaCu_2O_{8+\delta}$ (BSCCO) single crystal in relatively high external magnetic fields up to 200 mT. The observed flux distribution followed the Bean model. In addition to this general feature, we found an unexpected shift in the MFM data signal at certain specific external magnetic fields, which is discussed in detail.

II. SAMPLE PREPARATION AND EXPERIMENTAL SETUP

A BSCCO single crystal was grown by a floating zone method and was irradiated with 1.3 GeV uranium ions to form columnar defects parallel to the c axis.[5] The ion dose corresponds to a matching magnetic flux density of 2 mT. These artificial columnar defects act as strong pinning centers. Moreover, intrinsic line defects, which we identified as antiphase boundaries due to stacking faults[6] are present. They can accommodate a large number of vortices and exhibit an anisotropic pinning behavior, i.e., vortices are pinned strongly perpendicular to the line defect, but are very mobile along it. To compare our experiments with the Bean model in a simplified one-dimensional form, we cut the sample to a rectangular platelet of about $2a\times b\times c = 0.72\ \text{mm}\times 2.2\ \text{mm}\times 0.05\ \text{mm}$.

The low temperature magnetic force microscope setup is described elsewhere.[7] The only important point here is that the externally applied magnetic field $\mu_0 H_a = B_a$ is oriented parallel to the crystal c axis, i.e., normal to the sample surface (z axis). The magnetic tip was prepared by argon ion sputtering and evaporation of 20 nm iron on one triangular side face of the typically 10–15 μm high tip pyramid. These tips are exclusively sensitive to the z component of the magnetic stray field of the sample, because their magnetization is always aligned along the z axis. No significant bending of the cantilever has been observed in an external magnetic field up to 200 mT applied perpendicular to the sample surface.

All measurements have been performed using the frequency modulation technique described by Albrecht *et al.*[8] In this mode of operation the cantilever with eigenfrequency f_0 and force constant c_z is oscillated by a self-excitation resonance loop ("self-driven oscillator"). Due to the tip-sample interactions its actual resonance frequency f is shifted by Δf, i.e., $\Delta f = f - f_0$. When the amplitude A is much smaller than the decay length of the tip-sample interaction force, the frequency shift Δf is related to the derivative of the z direction interaction force F_z' as

$$\Delta f = -(F_z'/2c_z)f_0. \tag{1}$$

To image the topography, the tip scans over the sample relatively close to the surface (about 1 nm), while Δf is kept constant by a z feedback at its set point δf. For MFM measurements, we apply the plane-subtraction mode: In the topographic mode (feedback on), the sample slope is compensated by adding appropriate voltages to the z electrode of the

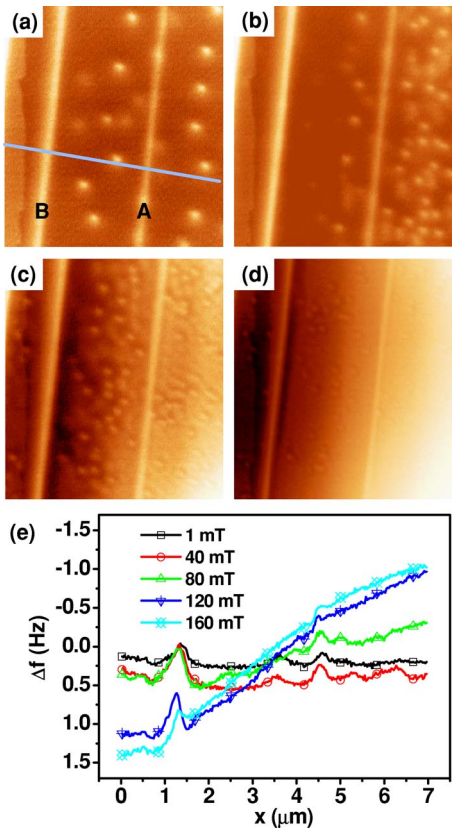

FIG. 1. (Color online) MFM images and line profiles obtained in the same area at several different external magnetic fields B_a=1 mT (a), 40 mT (b), 80 mT (c), 120 mT (d). The two bright stripes marked by A and B indicate the presence of a line defect acting as pinning center. (e) Profiles of each image and a not displayed image recorded at 160 mT obtained along the solid line in (a). More negative Δf values (upward y axis) indicate a larger MFM signal, i.e., larger flux density. One can notice that there are positive shifts (downward) in the Δf data on the left side of the line defects as the external field increases. Image parameters: f_0=204 kHz, c_z=52 N/m, A=10 nm, δf=−8 Hz, h=18 nm, T=5.2 K, a_{scan}=7 μm×7 μm.

sample scanner. Thereafter, the feedback is switched off, and the tip is retracted from the sample surface to a scanning height h of about 20 nm. A MFM image is obtained by scanning in this plane and recording the frequency shift, which is in this case dominated by long range magnetostatic force. If there is any slope in the MFM image, it is not due to the topographic slope of the sample but to the magnetic feature, because the topographic slope has already been compensated. According to the Bean model, flux lines distribute with a gradient related to the sample critical current density. In this sense, the gradient and signal value in the MFM image is important for the analysis of the data. We did not perform any image processing like plane flattening and offset nullifying for this reason, but used only raw data for our data analysis.

III. RESULTS AND DISCUSSION

Initially, the sample was field cooled (FC) in $B_a=B_{FC}$ =1 mT from above T_c down to 5.2 K. At 5.2 K, MFM images have been obtained with increasing magnetic field up to 160 mT in 5 mT intervals. Figures 1(a)–1(d) show several MFM images of the same scan area with B_a=1, 40, 80, and 120 mT, respectively. During the experiment, the direction of the tip magnetization was oriented parallel to B_a.

When the effective magnetic dipole of the tip is m_z and the z component of the magnetic induction at the tip position is B_z, the magnetic force F_z between tip and sample is given by $F_z=m_z\partial B_z/\partial z$ (dipole approximation). Then the frequency shift induced by this force is given by

$$\Delta f = -\frac{f_0 m_z}{2c_z}\frac{\partial^2 B_z}{\partial z^2}. \tag{2}$$

In case of single vortex, the polarity of $\partial^2 B_z/\partial z^2$ is the same as for B_z. Δf is negative when the vortex polarity (given by the direction of B_a) and tip magnetization are parallel as in our situation, where the tip-vortex interaction is attractive. In all our MFM images, brighter contrast represents more negative frequency shifts, whereby the vortices appear bright.

In Fig. 1(a) one can observe N=22 individual vortices in a scan area a_{scan} of 7 μm×7 μm. According to $B=N\cdot\Phi_0/a_{scan}$, this corresponds to a flux density of about 0.93 mT, which is smaller than B_{FC}. Moreover, two bright lines marked with A and B, respectively, are visible. As mentioned in the previous section, such bright lines are antiphase boundaries induced by stacking fault dislocations.[6] Due to the attractive tip-vortex interaction and the anisotropic pinning behavior the whole line defect appears bright, even though only a few vortices might be pinned at these line defects. Therefore, we assume that the missing flux is located at these two line defects. Note that the kinked surface step visible on the left side does not act as a strong pinning site.

With increasing external magnetic field, magnetic flux penetrates from the sample edges toward the center according to the Bean model. Since the scan area happens to be on the right side of the sample center, vortices enter it from the right side as seen in Fig. 1(b). At even higher external fields in Figs. 1(c) and 1(d), the vortex density in the scan area increases and for a vortex separation $r \ll \lambda$, individual vortices cannot be distinguished anymore. Many flux lines contribute to the tip-sample interaction. If the partial contributions of the ith vortex to the magnetic field and the frequency shift at the position of the tip magnetic moment are $B_{z,i}$ and Δf_i, respectively, the total frequency shift Δf can be expressed as a sum of each Δf_i like

$$\begin{aligned}\Delta f &= -\frac{f_0 m_z}{2c_z}\frac{\partial^2 B_z}{\partial z^2} \\ &= -\frac{f_0 m_z}{2c_z}\frac{\partial^2}{\partial z^2}\sum_i B_{z,i} \\ &= -\sum_i \frac{f_0 m_z}{2c_z}\frac{\partial^2 B_{z,i}}{\partial z^2} \\ &= \sum_i \Delta f_i. \end{aligned} \tag{3}$$

This implies that the MFM contrast due to each single vortex can be superposed. In this sense, the MFM image can

be considered to represent the flux density. Therefore, even at large flux densities where individual vortices cannot be distinguished anymore their distribution can still be detected.

Line profiles of each image obtained along the solid line parallel to the penetration direction as indicated in Fig. 1(a) are shown in Fig. 1(e). For 1 and 40 mT the profile is basically a horizontal line with some protrusions which correspond to individual vortices pinned either at a line defect or at a columnar defect. At higher B_a (80 and 120 mT), the MFM signal increases toward the right side of the image, reflecting the increasing vortex density toward the sample edges as predicted by the Bean model. For comparison, a profile obtained at the same line in a higher external field $B_a=160$ mT is also depicted to demonstrate the effect of the further increase of the external magnetic field. The slope in the flux distribution at $B_a=120$ mT remains nearly unchanged for $B_a=160$ mT. The constancy of the slope can be understood with the Bean model, where the slope is related to the magnitude of the critical current density J_c, which is an intrinsic property of the sample depending on the density of intrinsic pinning centers.

In fact, one can notice that the slope is not exactly spatially constant, but exhibits a fine structure. In particular, the flux density is increased at the locations of the line defects A and B, because they can accommodate a large amount of vortices. These repel other approaching ones, inhibiting their further advance, whereby the slope on the left side of line defect B is nearly horizontal. Comparison of the two line profiles obtained at 120 and at 160 mT reveals this fact more clearly. The flux density increases only on the right side of the line defects.

Another interesting point in the MFM profile is that there are frequency shifts toward positive Δf, as the external field increases. On the left side of the line defect B, the flux density can be considered to be negligible, since the line defect inhibits further flux penetration. The MFM signal in this region should remain unchanged with increasing external field as long as the incoming flux front has not arrived. In the MFM profiles shown in Fig. 1(e), however, the data on the left side of the line defect B are shifted to the direction of positive Δf with higher external field. This direction is indeed unexpected, since even though there had been a small amount of flux leakage through the line defect, the increased flux density should have yielded the more negative Δf due to the more attractive interaction between the tip and the flux.

A similar field ramping experiment was conducted in another region with a same type of line defect. MFM images were recorded continuously while B_a was ramped from 0 to 200 mT at a constant rate of 0.1 mT/s. The initial frequency shift was zero at $B_a=0$ mT. Figure 2(a) shows one of the MFM images, where the flux penetration across the line defect (visible as a bright line in the middle of the image) occurs. The image was obtained during ramping B_a from 182.5 mT (bottom) to 198 mT (top). The profiles displayed in Fig. 2(b) taken at 185.0, 188.5, and 192.0 mT, respectively, visualize the flux penetration and clearly show the difference between the flux distributions before and after flux penetration across the line defect. With increasing field, more vortices enter the scan area from the right side. In the shaded region of Fig. 2(b), one can observe the evolution of the

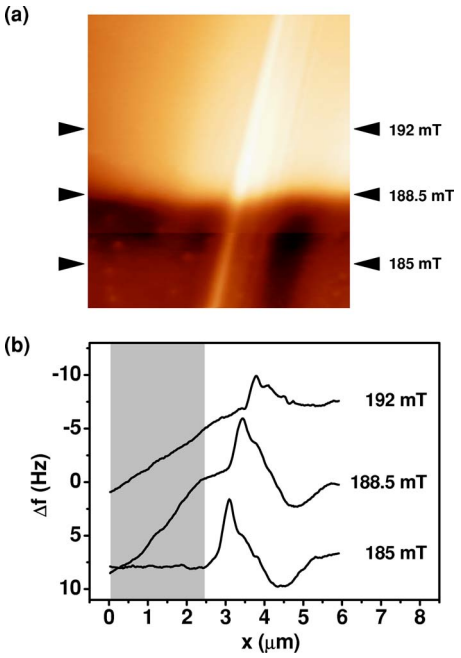

FIG. 2. (Color online) (a) MFM image obtained during B_a ramping from 182.5 mT (bottom of the image) to 198 mT (top of the image) at a constant rate of 0.1 mT/s. In the middle of the image at $B_a=188.5$ mT, the flux front begins to pass across the line defect. The MFM line profiles obtained at 185, 188.5, and 192 mT are displayed in (b), which clearly shows the difference between the flux distributions before and after flux-front propagation across the line defect. One can notice that the large positive shift in Δf observed at 185 mT (before the flux front passes through the line defect) disappears at 192 mT (after the flux front passes through the line defect). Image parameters: $f_0=69.7$ kHz, $c_z=2.2$ N/m, $A=20$ nm, $\delta f=-8$ Hz, $T=5.2$ K, $a_{scan}=6\times7$ μm^2.

flux-density profile on the left side of the line defect. Before flux penetration (185.0 mT), the vortices trapped in the line defect repel the incoming vortices, whereby there is a positive slope on the right side of the defect and a zero slope on the left side. As the incoming flux passes through the line defect (188.5 mT), the slope on the left side of the defect becomes positive. After the flux front passes by the line defect (192.0 mT), the flux distribution on the left side of the defect shows a positive constant slope, following the Bean model.

Considering the shifts of the data shown in Fig. 2, one can find that Δf shifts to the more negative direction after the flux-front passes through the imaging area, returning closer to the original Δf value at $B_a=0$ mT, i.e., 0 Hz. From the two experimental sets shown in Figs. 1 and 2, one can conclude that the observed data shift to the positive Δf is the largest when the flux front resides in the imaging area, that is, when there is a rather abrupt change in the slope of the flux density, e.g., due to the presence of a barrierlike line defect.

In addition to the above measurements for a constant tip-sample separation, the variations of Δf were also examined at different tip-sample distances up to 400 nm, which is the full z direction range of our scanner at 5.2 K. The positive Δf shift observed near the flux front did not vanish up to

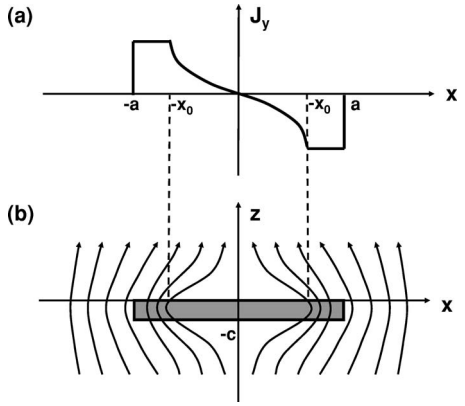

FIG. 3. (a) Distribution of y-direction current density J_y of a superconducting sample in transversal geometry, which follows the modified Bean model for transversal geometry formulated in Eq. (4). The position of the flux front is denoted as x_0. The features of the current density are different on each side of x_0. (b) Coordination of the sample of the transversal geometry with width $2a$ and thickness c. Magnetic field lines around the sample is also sketched. The external magnetic fields are shielded by the currents inside the sample. Close to the surface the flux lines exhibit a large in-plane component, which relaxes far away from the surface.

400 nm, which implies that it is due to an interaction of a very long range beyond 400 nm. Note that such a long-range magnetostatic interaction is usually not observed in MFM. For example, the emanating stray field of ferromagnets decays quickly due to flux closure between oppositely polarized domains. Therefore, usually only a small fraction of the total tip, i.e., its apex, interacts with the sample. However, the situation is different here. As one can see in Fig. 3(b), the external magnetic field is shielded due to the Meissner effect of the superconducting film. The shielding current flows around the whole sample area, yielding a very long-range variation of the magnetic field above the sample. To explain the observed shifts one has to consider the magnitude, direction, and origin of the total flux in the whole sample area, which is responsible for the frequency shift during MFM data acquisition.

The flux distribution in a superconducting specimen under an external magnetic field follows the so-called Bean model. This model neglects the discrete nature of the flux in superconductor, and assumes continuous distribution of flux and current density. Thus, it is not suitable for the analysis of the relatively short-range interaction between the magnetic flux emanating from an individual vortex and the apex region of the magnetic tip. However, as we will show in the following, the positive Δf shift originates from a very long-range interaction, where the whole 13 μm long iron coated tip side face of the tip has to be taken into account. Therefore, we can utilize the Bean model for our analysis. For transversal geometry, e.g., platelet sample in a perpendicular field, large demagnetizing factors play an important role, whereby the current density distribution is strongly modified compared to the original Bean model derived for longitudinal geometry. Brandt and Indenbom[9] and Zeldov *et al.*[10] reported a modified formula which holds for infinitely long strips. According to this formula, the current distribution inside the sample of width $2a$ (x direction), averaged along the sample thickness c (z direction) is given by,

$$J_y(x) = \begin{pmatrix} J_c, & (-a < x < -x_0) \\ -\frac{2J_c}{\pi}\arctan\left(\frac{x}{a}\sqrt{\frac{a^2-x_0^2}{x_0^2-x^2}}\right), & (-x_0 \leqslant x \leqslant x_0) \\ -J_c, & (x_0 < x < a) \end{pmatrix}. \tag{4}$$

Here x_0 is given by $x_0 = a\left[\cosh\left(\frac{\pi B_a}{\mu_0 c J_c}\right)\right]^{-1}$ and represents the position of the flux front. The above one-dimensional formula is also a good approximation for long rectangular shaped samples like ours (more than two times longer than wide). The distribution of the above y-direction current density $J_y(x)$ is depicted along the x direction in Fig. 3(a).

The z component of the magnetic flux $B_j(x,z)$ due to $J_y(x)$ can be calculated from Ampere's law, i.e.,

$$B_j(x,z) = \frac{\mu_0}{2\pi}\int_{-c}^{0}\int_{-a}^{a}\frac{J_y(u)(u-x)dudv}{(u-x)^2+(v-z)^2}. \tag{5}$$

The external applied magnetic field is shielded by the current distribution $J_y(x)$, yielding curved magnetic flux lines in the x-z plane as depicted in Fig. 3(b). The total magnetic flux density along the z-direction B_z is the sum of B_j and B_a. To be more specific, we estimated B_z with the parameters relevant for our sample and experimental condition: $a=360$ μm, $\mu_0 J_c = 10$ mT/μm, $c=50$ μm, and $B_a=200$ mT. The critical current density $\mu_0 J_c = 10$ mT/μm yields $J_c = 8.0\times 10^5$ A/m^2, which is quite similar to the reported value of the critical current density of BSCCO single crystal at around 5.2 K.[11] With these parameters, the position of flux penetration x_0 is at about 190 μm.

In Fig. 4(a), the model-calculated $B_z(x,z)$ is plotted with z in the range from 0.5 to 50 μm at several x positions from 130 to 250 μm, covering the region on both sides of the flux boundary $x_0 = 190$ μm.

One can notice a conspicuous difference in $B_z(x,z)$ between the positions at $x<x_0$ and at $x>x_0$. Close to the surface, the field distribution follows the Bean model. At $x<(x_0=190$ μm), the field is nearly shielded out, while the field increases linearly with x at a position $x>x_0$. Far away from the surface, the bent flux lines straighten, yielding a relatively large (small) B_z increase at $x<x_0$ ($x>x_0$).

To compare this model calculation with the MFM data, one has to consider that the MFM signal is related to the second derivative of the magnetic induction B_z'' by Eq. (2). The slope variations of each curve shown in Fig. 4(a) represent the second derivative of B_z. They are plotted in Fig. 4(b) for three exemplary values, i.e., $x=170$ μm ($<x_0$), 190 μm ($=x_0$) and 210 μm ($>x_0$). At $x<x_0$ and $x>x_0$, the slope of B_z is nearly constant, yielding vanishing B_z''. At around $x \simeq x_0$, however, the slope of B_z becomes smaller with increasing distance z, yielding a negative B_z''. The above model-calculation shows that B_z'' changes abruptly at around $x \simeq x_0$ with a large negative peak at $x=x_0$. Such a behavior of B_z'' would result in a shift toward more positive Δf values in the MFM signal by Eq. (2).

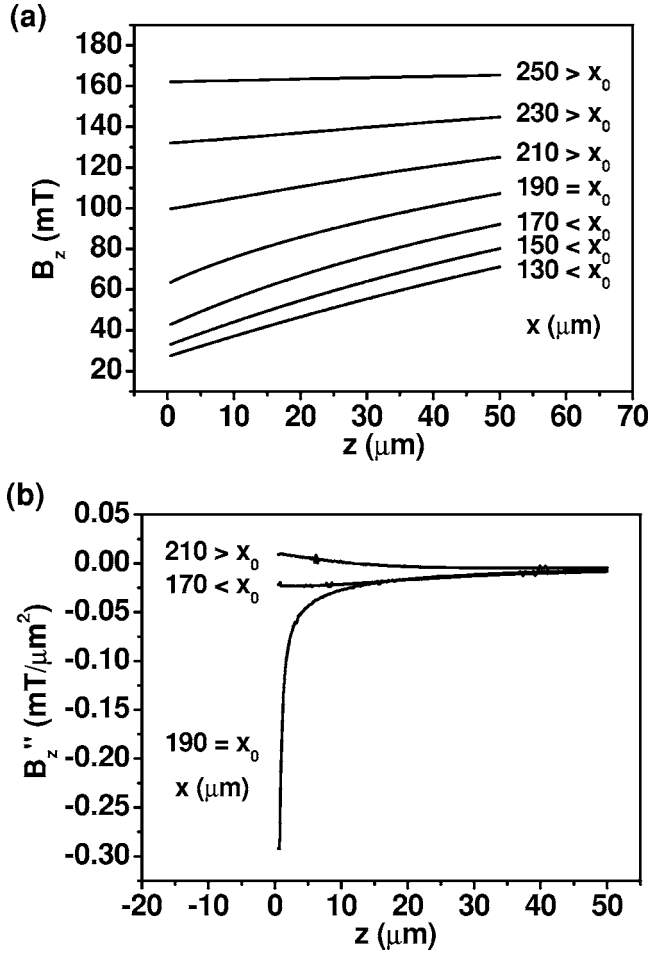

FIG. 4. (a) $B_z(x,z)$ versus z curves at several different x values on both sides of the flux front at $x_0=190$ μm. The curves are calculated with appropriate experimental parameters from the model flux distribution according to the transversal Bean model. One can notice that the curvature of B_z changes distinctively at the position of the flux-front $x=x_0$. (b) Plot of second derivative B_z'' of the model-calculated B_z obtained at several x values of 170, 190, and 210 μm. Note that for dynamic mode MFM this is the measured physical quantity, since $\Delta f \propto F_z' \propto B_z''$. Its magnitude is relatively small at $x=170$ μm ($x<x_0$) and $x=210$ μm ($x>x_0$), while it has a large negative value directly at $x=x_0=190$ μm.

In our experiment, the position of the flux-front x_0 is changed by the increasing external magnetic field B_a, while the position of the imaging area x remains constant. For the experimental data set shown in Fig. 1, the flux front can be considered to reach the scan area at $B_a \simeq 120$ mT, since there is an abrupt slope change at this field as shown in Fig. 1(e). The observed positive shift of the Δf data at $B_a=120$ mT in Fig. 1(e) can be understood from the negative B_z'' at around $x=x_0$ found in the model calculation as described above.

The situation is slightly different in Fig. 2, where the slope change is enhanced due to the line defect in the middle of the image, which functions as a strong pinning site. However, even in this case, the above analysis can be applied qualitatively, because there are large differences in the slope of the flux density between each side of the line defect. The position of the flux-front x_0 can be considered to reach the imaging area x at an external field $B_a=185$ mT. Beyond this field, the flux front begins to penetrate through the flux barrier of the line defect, and the slopes on both sides of the line defect become similar. This corresponds to a situation of $x>x_0$ in the model calculation. The maximal shift of B_z'' at around $x=x_0$ becomes smaller after the flux front passes through the imaging area. This behavior agrees well with the observed Δf shift shown in the line profiles in Fig. 2(b). At $B_a=185$ mT ($x=x_0$), the Δf shifts maximally to the positive direction, and becomes more and more negative as the field increases ($x>x_0$), approaching to the original Δf value, i.e., zero.

From the model-calculated B_z'' curves shown in Fig. 3(b), the derivative of the tip-sample interaction force F_z' can be estimated using an appropriate tip magnetic moment parameter m_z. According to the specifications of the manufacturer, our tip can be considered as a 20 nm thick iron (saturation magnetization$=1.7\times10^6$ A/m) triangular slab with a base length of 10 μm and a height of 13 μm. By integrating B_z'' with a weighting factor defined by the triangular slab geometry, we could estimate the force derivative F_z' at $x=x_0$ to be -1.55×10^{-4} N/m. The corresponding Δf can be calculated from Eq. (1), yielding 0.3 and 2.4 Hz in the two experiment sets shown in Figs. 1 and 2, respectively. The observed Δf shifts in Figs. 1 and 2 are 1.3 and 8 Hz, respectively. The expected values from the model calculation are about four times smaller than the observed Δf shifts. In the model calculation, we did not take into account the effect of the line defect that inhibits further advance of the flux. The larger Δf observed in the experiment must be due to the enhanced difference of the flux density on each side of the line defect. Actually, considering that the parameters for the model calculation can only roughly be estimated, such a discrepancy is not surprising.

IV. SUMMARY

We visualized the flux distribution in rather high external magnetic fields, where the intervortex distances are much smaller than λ and individual vortices cannot be distinguished anymore by MFM. Unexpected shifts of the MFM signal were observed around advancing flux fronts during magnetization of a BSCCO platelet crystal and close to the defect induced transition regions between high and low flux densities. The effect could be explained by considering the current density according to the transversal Bean model and the resulting magnetic flux density distribution. In addition to a qualitative description of the phenomenon, reasonable agreement with the magnitude of the measured data shifts was achieved by taking the origin of the dynamic mode MFM-signal, i.e., $\Delta f \propto B_z''$ (dipole approximation) into account. Our result should facilitate interpretation of MFM data obtained on superconductors.

ACKNOWLEDGMENTS

Financial support by the NSI-NCRC program of KOSEF in Korea and from the DFG (Graduiertenkolleg Physik nanostrukturierter Festkörper) in Germany is gratefully acknowledged.

*Present address: Rheinisch-Westfälische Technische Hochschule (RWTH) Aachen, Department of Physics, 52056 Aachen, Germany.

[1] A. Moser, H. J. Hug, I. Parashikov, B. Stiefel, O. Fritz, H. Thomas, A. Baratoff, H.-J. Guntherodt, and P. Chaudhari, Phys. Rev. Lett. **74**, 1847 (1995).

[2] M. Rosemann and P. Grutter, New J. Phys. **3**, 24 (2001).

[3] A. Volodin, K. Temst, C. Van Haesendonck, and Y. Bruynseraede, Appl. Phys. Lett. **73**, 1134 (1998).

[4] U. H. Pi, Z. G. Khim, D. H. Kim, A. Schwarz, M. Liebmann, and R. Wiesendanger, J. Low Temp. Phys. **131**, 993 (2003).

[5] T. W. Lee, C. W. Lee, S. Y. Shim, D. H. Ha, and D. H. Kim, Progress in Superconductivity **3**, 36 (2001).

[6] U. H. Pi, Z. G. Khim, D. H. Kim, A. Schwarz, M. Liebmann, and R. Wiesendanger, Phys. Rev. B **69**, 094518 (2004).

[7] M. Liebmann, A. Schwarz, S. M. Langkat, and R. Wiesendanger, Rev. Sci. Instrum. **73**, 3508 (2002).

[8] T. Albrecht, P. Gruetter, D. Horne, and D. Rugar, J. Appl. Phys. **69**, 668 (1991).

[9] Ernst Helmut Brandt and Mikhail Indenbom, Phys. Rev. B **48**, 12893 (1993).

[10] E. Zeldov, Joh R. Clem, M. McElfresh, and M. Darwin, Phys. Rev. B **49**, 9802 (1994).

[11] V. V. Metlushko, G. Guntherodt, P. Wagner, H. Adrian, I. N. Goncharov, V. V. Moshchalkov, and Y. Bruynseraede, Appl. Phys. Lett. **63**, 2821 (1993).